Near-Surface Frontal Zone Trapping and Deep Upward Propagation of Internal Wave Energy in the Japan/East Sea

ANDREY Y. SHCHERBINA AND LYNNE D. TALLEY

Scripps Institution of Oceanography, University of California, San Diego, La Jolla, California

ERIC FIRING AND PETER HACKER

Department of Oceanography, University of Hawaii at Manoa, Honolulu, Hawaii

(Manuscript received 20 December 2001, in final form 15 October 2002)

ABSTRACT

The full-depth current structure in the Japan/East Sea was investigated using direct velocity measurements performed with lowered and shipboard acoustic current Doppler profilers. Rotary spectral analysis was used to investigate the three-dimensional energy distribution as well as wave polarization with respect to vertical wavenumbers, yielding information about the net energy propagation direction. Highly energetic near-inertial downward-propagating waves were found in localized patches along the southern edge of the subpolar front. Between 500- and 2500-m depth, the basin average energy propagation was found to be upward, with the maximum of relative difference between upward- and downward-propagating energy lying at about 1500-m depth. This difference was most pronounced in the southeastern part of the basin.

1. Introduction

The Japan Sea (also known as the East Sea) is a marginal sea of the northwestern Pacific, separated from the open ocean by the islands of Honshu, Hokkaido, and Sakhalin (Fig. 1a). It consists of three fairly deep basins: the Japan basin in the north being the deepest (over 3500-m depth), and the Ulleung and Yamato basins (over 2000-m depth) in the southwest and southeast respectively, separated by the Yamato rise at about 39°N, 135°E. The connection with the open ocean is through four straits less than 200 m deep: Tsushima strait in the south and Tsugaru, Soya and Tatar straits in the northeast.

The circulation in the Japan Sea consists of two well-defined gyres, separated by the subpolar front at about 40°N. A branch of the Kuroshio Current enters through Tsushima Strait as two jets along either side of Tsushima Island: the East Korea Warm Current (EKWC) through the western channel (major part of the inflow) and the Tsushima Current (TC) through the eastern one (Perkins et al. 2000). Both total inflow and relative transports of the branches vary significantly in time around a mean value of 2 Sv (Sv $\equiv 10^6$ m^3 s^{-1}). The EKWC forms a western boundary current along the coast of the Korean peninsula. It separates from the coast at 37°–39°N, where it meets the southward-flowing North Korea Cold Current (NKCC). This confluence forms the subpolar front that extends eastward as a series of meanders and mesoscale eddies (Fig. 1c).

The Tsushima Current, joined by a few countercurrent branches of the EKWC, continues northeastward along the coast of Japan, generally following the jagged topography of the coastline and continental slope, giving rise to high mesoscale eddy variability in the Yamato Basin. The outflow through Tsugaru Strait provides a small but important input of warm saline water into the Kuroshio–Oyasho mixed water region east of Honshu (Talley 1991).

Long-term mooring observations (Takematsu et al. 1999b) have shown a high level of internal wave energy in the Japan Sea with a sharp peak at the inertial period of about 18 h. The most energetic inertial oscillations were observed in moorings located in the central parts of the Japan Sea and in the vicinity of the subpolar front. Unfortunately, the sparse mooring coverage could not provide much detail regarding the spatial variations in the near-inertial wave field. However, such variations might be anticipated, given the strong mesoscale variability in the region which can modulate the internal wave field (e.g., Mooers 1975a).

In summer 1999 a comprehensive hydrographic survey of the Japan Sea was conducted with the objective

Corresponding author address: Andrey Shcherbina, Physical Oceanography Research Division, Scripps Institution of Oceanography, University of California, San Diego, 9500 Gilman Dr., La Jolla, CA 92093-0230.
E-mail: ashcherbina@ucsd.edu

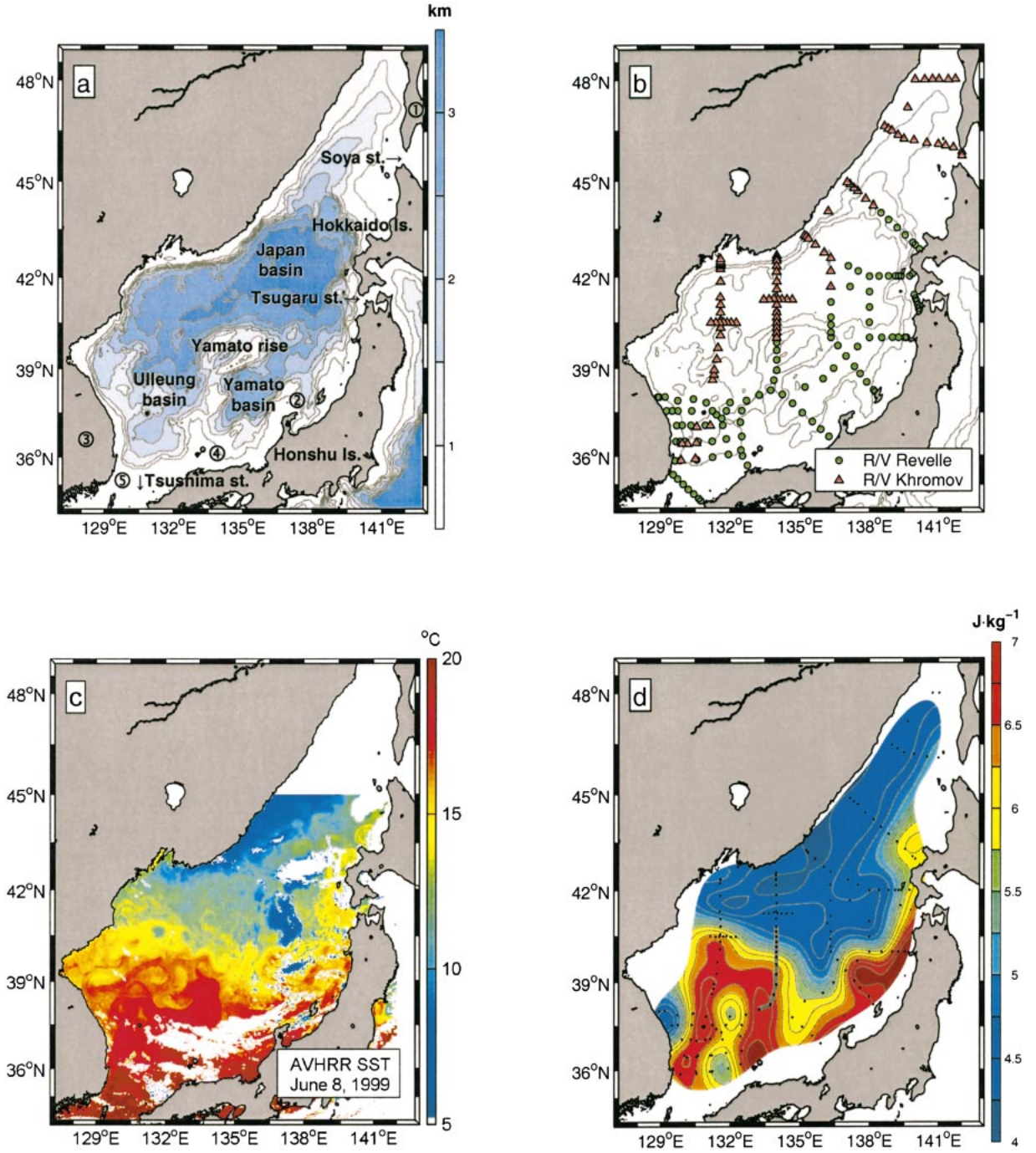

FIG. 1. (a) Map of the Japan/East Sea. Numbers indicate (1) Sakhalin Island, (2) Noto Peninsula, (3) Korean Peninsula, (4) Oki Island, and (5) Tsushima Island. (b) Cruise tracks and station positions for R/V *Revelle* (24 Jun–17 Jul 1999) and R/V *Professor Khromov* (22 Jul–11 Aug 1999). (c) AVHRR sea surface temperature snapshot (courtesy of R. Arnone and S. Ladner, Naval Research Laboratory, Stennis Space Center). (d) Dynamic height at the sea surface relative to 500 m. Also shown is the cross-frontal section used in subsequent figures (gray line).

of obtaining ''a complete synoptic view of the vertically layered structure and major components of the circulation'' of the basin. The survey included a series of field experiments to study local features including the Tsushima and Liman Currents, the subpolar front, and eddy structures. A distinctive feature of the project was the extensive use of shipboard and lowered acoustic Doppler current measurements to gather a first (to our knowledge) comprehensive set of velocity profiles covering most of the Japan Sea basin and extending to the

bottom. In this paper, the velocity measurements are analyzed to infer the horizontal and vertical distribution of internal wave energy in the basin, with particular attention paid to variations in the internal wave field in the frontal zone.

2. Data

The Japan Sea survey was made with two ships. The southern part of the Japan Sea was covered by R/V *Revelle* (Scripps Institution of Oceanography, United States) between 24 June and 17 July 1999; the survey was continued in the northern and northeastern regions by R/V *Professor Khromov* (Far Eastern Regional Hydrometeorological Research Institute, Russia) from 22 July to 11 August 1999. A total of 203 stations were occupied with CTD/Rosette sampling for temperature, salinity, oxygen, nutrients, chloroflurocarbons, and other tracers (Fig. 1b).

The CTD/Rosette used on most stations (with the exception of three casts during severe weather conditions) was equipped with a lowered acoustic Doppler current profiler (LADCP). With the exception of four stations inside eddies in the Japan Basin, every station extended to within 20 m of the bottom, with most within 10 m.

The LADCP is a self-contained broadband 150-kHz RD Instruments ADCP mounted on a standard rosette frame. This configuration provides top-to-bottom velocity profiling with each CTD cast (Firing and Gordon 1990). As the instrument is being lowered and then hoisted back at the station, the ADCP records water velocities within its range approximately every second. As the ADCP used lacks a pressure sensor, the record is synchronized with the CTD pressure time series. The set of velocity profiles, overlapping in depth, is converted to vertical shear and averaged in 5-m depth bins. This procedure is necessary to remove the time varying (but constant for each individual profile) bias in the velocity data, induced by the movement of the package through the water. The shear profile is then integrated and combined with the GPS navigation data during the cast to get an absolute velocity profile (Fischer and Visbeck 1993). Instrument characteristics prevent reliable measurements within about 45 m from the bottom or 30 m from the surface.

The present study relies upon vertical shear data, which is less susceptible to error than the absolute velocity profiles, as the latter additionally requires accurate navigation data. P-code GPS navigation was available for most of the first cruise (R/V *Revelle*). For the second cruise (R/V *Khromov*) the shipboard GPS record was noisy and intermittent. A separate GPS record from an independent onboard meteorological station was used to bridge the gaps (data provided by R. Limeburner, Woods Hole Oceanographic Institution). Nonetheless, low accuracy of navigational data was characteristic of the second part of the survey. Additionally, strong onstation drift of the *Khromov* occasionally led to the tilt of the LADCP package beyond the measurable range of 20°, invalidating fragments of a few profiles. As a result, errors in excess of 30 cm s^{-1} in the absolute velocity were found on several *Khromov* stations. Because of a large number of factors affecting the calculation procedure, such errors are sometimes difficult to recognize and quantify. The shear data, however, were unaffected by these problems. A total of 19 LADCP profiles (10 for the first cruise and 9 for the second one) were excluded from the analysis because of severe gaps in shear or inconsistencies between the up- and downcasts.

R/V *Revelle* is also equipped with a 150-kHz shipboard ADCP that provided underway velocity measurement with 5-min sampling interval and 8-m vertical resolution. For most of the cruise the concentration of scatterers in the water allowed reliable velocity measurements to about 300-m depth. The ADCP data were processed using the Common Oceanographic Data Access System (CODAS) software package. No shipboard ADCP data were available during the *Khromov* cruise.

3. Trapped internal waves in the subpolar front region

a. Background

The subpolar front in the Japan/East Sea extends across the basin at about 40°N and is visible in both temperature and salinity fields. The front is observed throughout the year, but its latitude varies with season. In the synoptic sea surface temperature field (Fig. 1c) from the Advanced Very High Resolution Radiometer (AVHRR) on 8 June 1999, about two weeks prior to the start of the survey, the front is clearly visible at its summer position between 39° and 40°N. This satellite image also shows the complex structure of the frontal zone, consisting of a number of meanders and mesoscale eddies. Such structure is characteristic of all synoptic images of the front. The front is apparent in the CTD survey also. Dynamic height at the sea surface relative to 500 m (Fig. 1d) shows the front at 40°N looping to the south at 135°E.

In course of the survey, two overlapping cross-frontal sections along 134°E were occupied. The first, occupied 2–4 July 1999, from the *Revelle,* is shown in Fig. 1d by a gray line. On 6 August 1999, the part of the section north of 40°N was repeated from the *Khromov.* The subpolar front is visible in the geostrophic velocity relative to 500 m (Fig. 2a) as a pair of closely spaced eastward-flowing jets at about 40°N with a maximum speed of about 30 cm s^{-1}, decaying rapidly with depth. An elongated anticyclonic eddylike feature is evident south of 38.5°N.

LADCP and shipboard velocity measurements taken in the frontal zone show much more complicated vertical structure than that suggested by geostrophy. In partic-

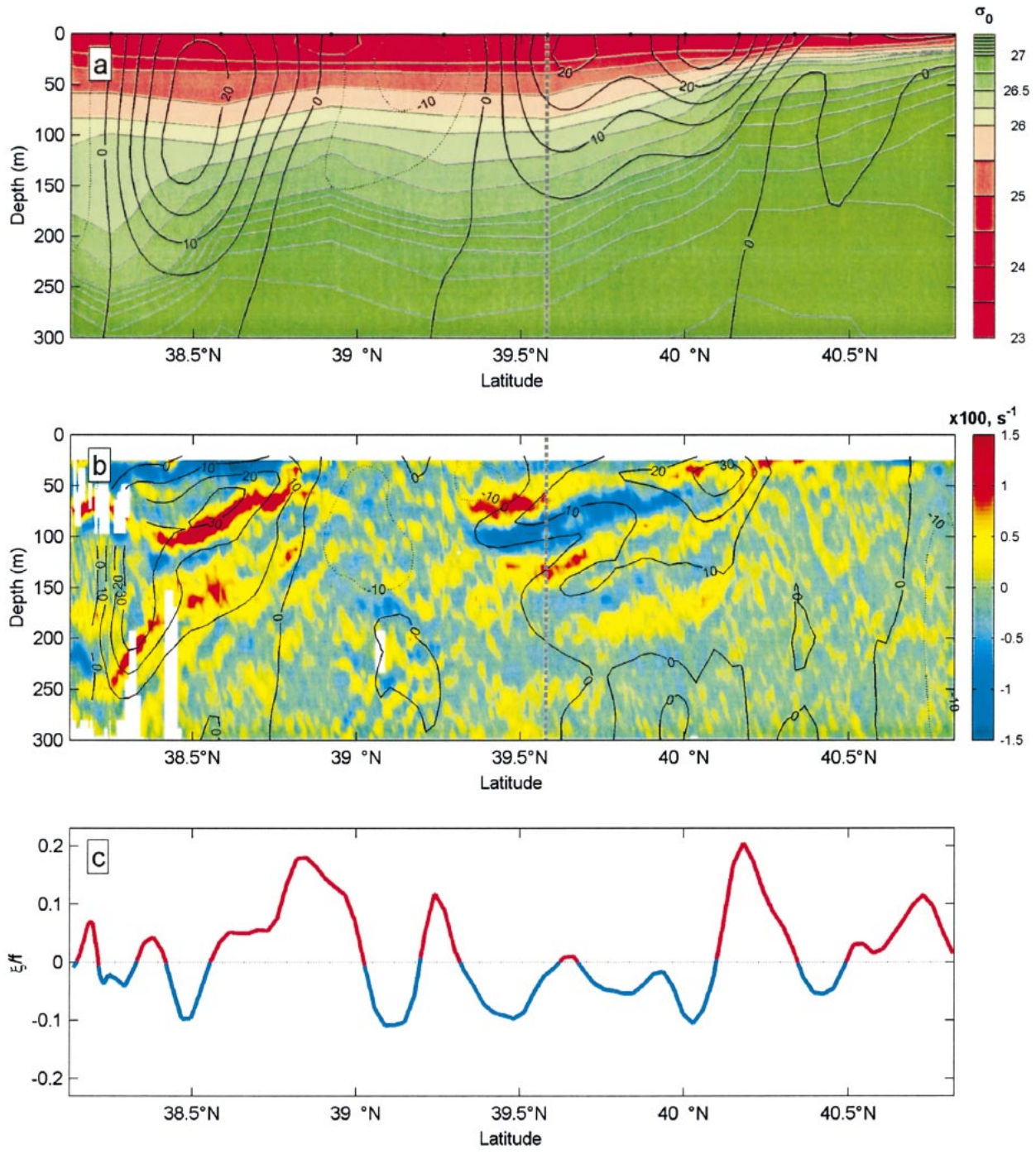

FIG. 2. (a) Potential density on a cross-frontal section, 2–4 Jul 1999. Black contours show geostrophic velocities relative to 500 m (cm s^{-1}, positive eastward). (b) Zonal component of back-rotated ADCP shear on the same section. Black contours show cross-sectional ADCP velocity (cm s^{-1}, positive eastward). (c) Mean relative vorticity in the upper 100 m, estimated as the along-track derivative of the cross-track ADCP velocity component. The section runs N–S north of 39°N and gradually turns to SE toward the southern end (Fig. 1d). Vertical dashed line indicates the position of the station used in Fig. 3.

ular, a distinctive spiral velocity pattern was observed at three stations on both occupations in close proximity to the front, including one on the southern edge of the front at 39°35′N, 134°E from the first occupation (Fig. 3). Eastward geostrophic flow associated with the front and reaching 18 cm s^{-1} at the surface is modulated by a spiral with the amplitude exceeding 10 cm s^{-1} (Fig. 3b). This spiraling vertical velocity profile suggests a

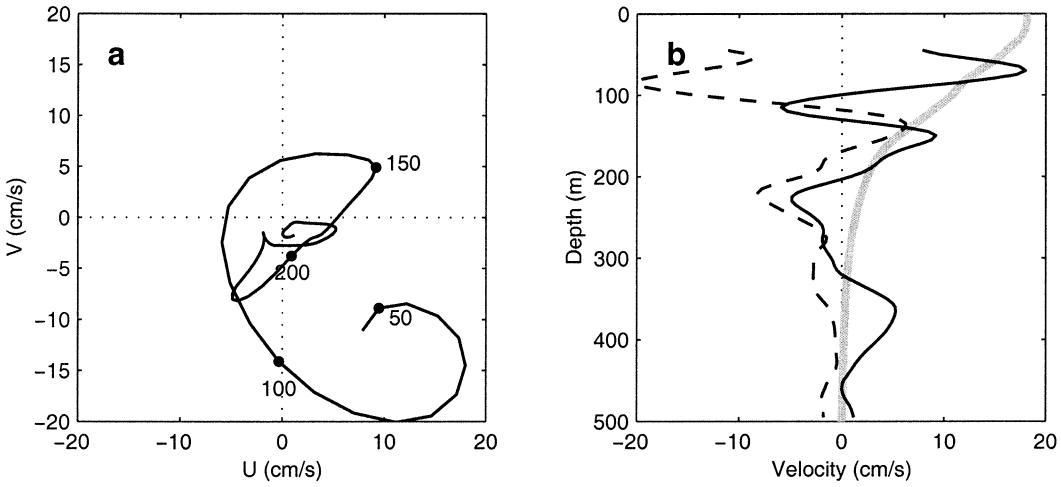

FIG. 3. (a) Velocity hodograph, with numbers indicating depth in meters, and (b) zonal (U, solid line) and meridional (V, dashed line) velocity profiles at a station (39°35′N, 134°E) inside the frontal zone (station position in Fig. 2). The geostrophic velocity profile relative to 500 m is shown for comparison (heavy gray line).

strong internal wave present in the upper 200 m. The velocity vector turns clockwise with increasing depth (Fig. 3a), indicating downward group velocity (Leaman and Sanford 1975). Total internal wave kinetic energy integrated over the upper 200 m is estimated to be of order of 1 kJ m^{-2}.

Such large-amplitude spiraling was observed only at the three stations inside the frontal zone between 39.5° and 40°N and not at any other locations in the survey. Significant but weaker clockwise spiraling is also present in the LADCP velocity profiles on the periphery of the anticyclonic feature in the southern part of the section. However it is much less obvious than in the frontal zone, and special analysis was necessary to extract that signal (see section 4 below).

b. Previous studies

Areas of strong geostrophic flows such as frontal zones are known to alter significantly the behavior of internal waves. As was shown by Fomin (1973) and Mooers (1975a), the primary effect of large-scale relative vorticity $\zeta = V_x - U_y$ is to shift the lowest internal wave frequency from the Coriolis frequency f to an effective Coriolis frequency $f_{\text{eff}} = f + \zeta/2$. Such a shift creates waveguide conditions in the regions of negative relative vorticity that may lead to the trapping of near-inertial waves (Mooers 1975a,b; Olbers 1981). Kunze (1985) applied Wentzel–Kramers–Brillouin (WKB) ray theory to demonstrate the existence of such a three-dimensional waveguide associated with a baroclinic jet. By trapping here we understand not only inability of subinertial internal waves with the frequencies between f_{eff} and f to leave a negative vorticity region, but also concentration of near-inertial wave energy in such regions because of the diminishing group velocity (Kunze 1985).

Previous observations confirmed enhanced levels of downward-propagating internal wave energy in regions characterized by significant negative vorticity, such as the warm (southern) sides of the North Pacific Subtropical Front (Kunze and Sanford 1984), and the Sargasso Sea front (Mied et al. 1986).

c. Shear structure across the front

According to the above theories, significant variations in the internal wave field could be expected in conjunction with varying large-scale vorticity across the front. Such variations were studied using cross-frontal section of vertical shear, based on shipboard ADCP data (Fig. 2b).

To estimate the synoptic shear in a cross-frontal section occupied during 36 hours, we have to back-rotate the observed shear to a common time, t_0:

$$\tilde{u}_z + i\tilde{v}_z = (u_z + iv_z)\exp[i\omega(t - t_0)],$$

where the tilde denotes the estimate at t_0, u_z, and v_z are zonal and meridional components of shear, and ω is the frequency of the dominant internal wave mode. Unfortunately, existing data do not allow direct estimate of the temporal frequencies since each station was occupied only once and each cast took less than two hours. Consequently, we have to make an ad hoc assumption that the observed shear structures are associated with a near-inertial wave ($\omega \approx f$), similar to that observed by Kunze and Sanford (1984) in the North Pacific Subtropical Front. Consistent with this assumption, back-rotation with inertial frequency f eliminates most of the discontinuities in the shear section that would have resulted from 1–2 hour station stops (Fig. 2b). Some discontinuity can still be observed outside the coherent part of the internal wave packet, where higher-frequency internal waves dominate (e.g., at 39.3°N). As was noted

by an anonymous reviewer, the strong horizontal coherence of the shear structures over scales of over 50 km is another indication of the near-inertial nature of the observed internal wave.

An internal wave packet with group velocity directed obliquely southward and down appears to be trapped at the warm (south) side of the front (39.3°–40°N). Vertical and horizontal wavelengths of the wave are approximately 75 m and 38 km, respectively, which corresponds to a wave frequency $\omega = 1.02f$ (provided there is no cross-section phase velocity component, and using the buoyancy frequency $N \sim 100f$ observed at 100 m). The scales of the trapped near-inertial wave, as well as its location in the region of negative large-scale vorticity (Fig. 2c) on the southern edge of the front are similar to observations at the North Pacific Subtropical Front (Kunze and Sanford 1984).

Another example of internal wave trapping is associated with the periphery of the anticyclonic feature situated to the southeast of the section (38.3°–39°N). However, in this instance the observations suggest that the trapping actually occurs in the region of positive vorticity (Fig. 2c). It should be noted that large-scale vorticity could only be estimated as along-track derivative of the cross-track velocity. Even though this estimate is likely a valid approximation for the frontal region characterized by a strong steady jet perpendicular to the section, this estimate is incomplete on the section leg tangential to the eddylike feature (38.5°–39°N). Consequently, we are unable to determine whether the internal wave energy concentration in this region contradicts the theoretical considerations of section 3b.

d. Rotary spectrum

Figure 4 shows a vertical rotary spectrum computed using 98 consecutive 5-min shipboard ADCP shear profiles, all located in the frontal zone between 39.3° and 40.1°N down to 300 m, that is, the region with the strongest manifestation of the near-inertial wave. For comparison, a background internal wave energy spectrum (computed using the same number of ADCP profiles just north of the front, between 40.1° and 40.5°N) is shown in dashed lines. Uncertainty analysis is described in the appendix.

While background spectra show no significant difference between CW and CCW components, CW energy dominates in the frontal zone. For wavelengths close to 100 m it exceeds CCW energy by more than an order of magnitude.

e. Change in polarization across the front

Integration of vertical spectra $S(k_z)$ over wavenumber domain allows separation of the total baroclinic kinetic energy into clockwise and counterclockwise parts:

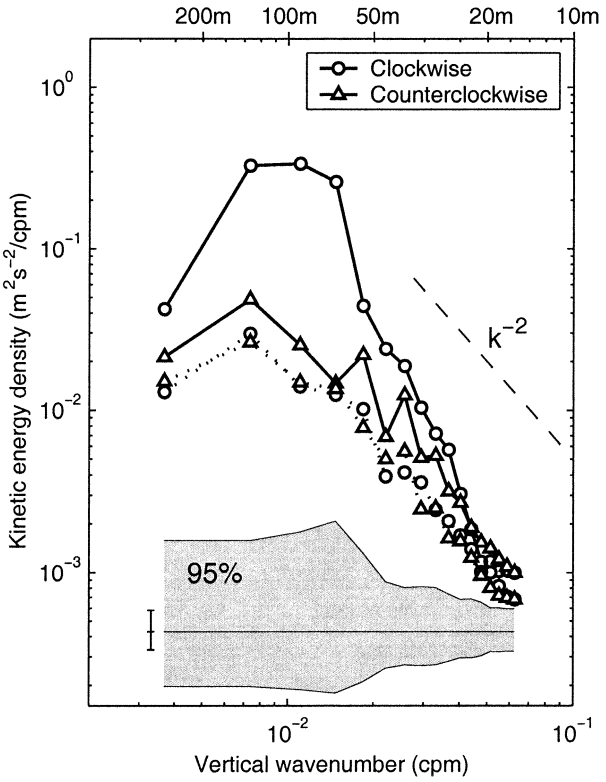

FIG. 4. Vertical rotary spectrum of horizontal velocity inside the frontal zone (solid lines) and north of it (dashed lines). Clockwise (circles) and counterclockwise (triangles) components are shown. Shading shows 95% confidence interval (see appendix for details).

$$E_{\mathrm{CW}} = \int_{-k_{\max}}^{0} S(k_z)\, dk_z;$$

$$E_{\mathrm{CCW}} = \int_{0}^{k_{\max}} S(k_z)\, dk_z, \qquad (1)$$

where $k_{\max}$ is the cutoff wavenumber. As was shown by Leaman (1976), the difference between E_{CW} and E_{CCW} gives the net energy difference between downward- and upward-propagating internal waves. Figure 5 shows the results of such integration of rotary spectra of the ADCP and LADCP profiles on a cross-frontal section.

Prior to integration, LADCP spectra were corrected to compensate for the smoothing and interpolation involved in LADCP processing (Polzin et al. 2002), using the model spectral transfer function

$$T_M(k_z) = \mathrm{sinc}^{10}\left(\frac{k_z \Delta z_r}{2\pi}\right) \mathrm{sinc}^{4}\left(\frac{k_z \Delta z_g}{2\pi}\right),$$

where $k_z = 2\pi/\lambda_z$ is the vertical wavenumber, Δz_r is LADCP bin length (16 m), and Δz_g is the vertical grid spacing (5 m). Polzin et al. (2002) have shown that such correction ''removes much of the discrepancy for vertical wavelength larger than 50 m'' (between LADCP and concurrent expendable current profiler spectra). In

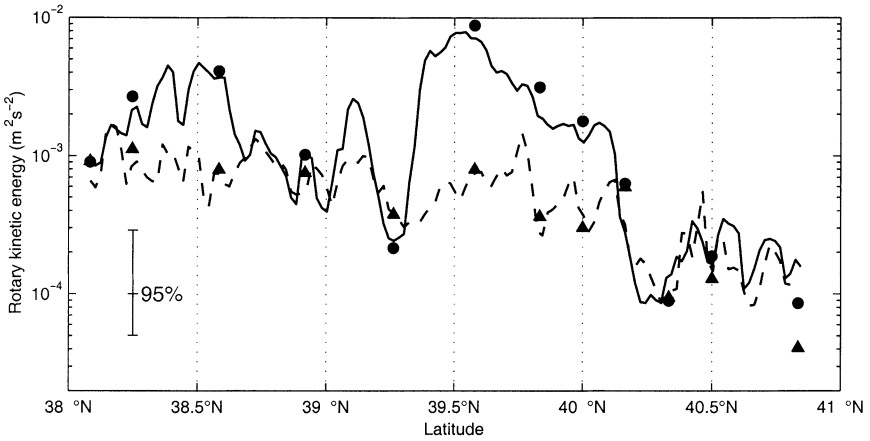

FIG. 5. Clockwise and counterclockwise energies on a cross-frontal section (location in Fig. 1d) at depths between 50 and 300 m based on shipboard ADCP (solid and dashed lines respectively) and LADCP stations (circles and triangles respectively). 95% confidence intervals are shown (see appendix for details).

order to reduce leakage, prewhitening of LADCP data was employed by calculating the shear spectrum $S_z(k_z)$ first and then recovering the energy spectrum using another response function

$$T_D(k_z) = k_z^2$$

so that the corrected spectrum is given by

$$S^{\text{corr}}(k_z) = \frac{S_z(k_z)}{T_M(k_z)T_D(k_z)}. \quad (2)$$

The cutoff wavenumber $k_{\max}$ was set to 0.13 rad m^{-1} ($\lambda_z = 50$ m), above which the LADCP resolves no useful signal (Polzin et al. 2002).

Because of smaller bin length (8 m) and less intensive processing, the correction (2) was not applied to the shipboard ADCP spectra and $k_{\max}$ in (1) was set to the maximum resolvable (Nyquist) wavenumber. The energies estimated from the ADCP profiles were mapped to regular 1-min latitude intervals.

The increase in the energy of downward-propagating waves south of the front (39.3° and 40.1°N) corresponds to the near-inertial waves trapped in the regions of negative vorticity. The level of total baroclinic energy is lower north of the front. Figure 4 shows that the increase in energy levels south of the front is observed over a wide range of wavenumbers, although this effect can in part be attributed to the spectral leakage from poorly represented large-scale vertical shear.

Although the LADCP (Fig. 5) may misrepresent the internal wave energy as a result of poor response at higher wavenumbers, the estimate of E_{CW} and E_{CCW} separation is consistent with that inferred from ADCP data. Therefore, LADCP profiles appear to be quite suitable for a study of horizontal and vertical energy distribution for the whole of the Japan Sea as presented in the next section since shipboard ADCP data penetrate to only 300 m and were also not collected in the northern Japan Sea.

f. Discussion

In order to study the source of the near-inertial wave energy in the frontal zone, a simple slab mixed layer model (D'Asaro 1985) was used to estimate the energy flux from wind to near-inertial waves in the ocean.

The characteristic mixed layer depth observed by the CTD survey was 25 m south of the front and 15 m north of it. The former value was used as a constant mixed layer depth in the model. The model's damping parameter r was set to 1 day^{-1}. The model was driven by wind stress computed from the four-times-daily National Centers for Environmental Prediction (NCEP) global reanalysis wind data using the Large and Pond (1981) drag coefficient and spline-interpolated on a half-hour grid. Despite its low temporal resolution, such forcing allows adequate estimation of near-inertial energy flux variation (Alford 2001). The effect of the coarse sampling was estimated by comparing the response of the model, forced with high-resolution windstress time series, subsampled at various intervals (D'Asaro 1985). Using both synthetic (steady wind rotating at the local inertial frequency) and realistic (5-min shipboard wind speed data) time series, we found that 6-hour sampling results in 20%–40% underestimation of energy flux. Nevertheless, the model should be sufficient for qualitative analysis. The model was run for the whole basin, with the particular attention paid to the NCEP grid point located 128 km west of the cross-frontal section (Fig. 6), with this choice justified below.

The first cross-frontal section was occupied on 2–3 July, about a week after the passing of a moderate storm with a pressure low of 1002 hPa along the southeastern edge of the basin on 24–25 June. The model indicates injection of about 700 J m^{-2} of the inertial wave energy into the mixed layer over the course of these two days, which is consistent with the total kinetic energy of the near-inertial wave observed (1 kJ m^{-2}; see section 3a),

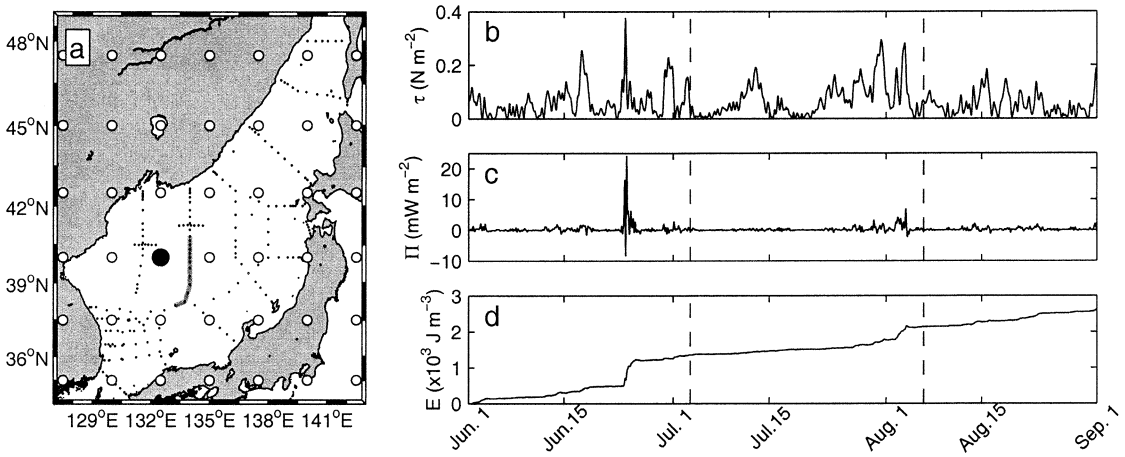

FIG. 6. (a) NCEP grid points over the Japan/East Sea (open circles). The large solid circle indicates the grid point chosen for analysis. Survey station positions are shown as small dots. The cross-frontal section used in Figs. 2 and 5 (gray line) is also shown. (b) Absolute windstress for Jun–Aug 1999, calculated from NCEP data. (c) Estimated near-inertial energy flux. (d) The time integral of the near-inertial energy flux. Vertical dashed line shows the times of the front crossings.

especially taking into account deficiencies of model forcing. The time record indicates that this storm was the only significant inertial forcing event in central Japan/East Sea for at least a month prior to the observations being made, which suggests that it was solely responsible for the generation of the observed near-inertial waves. Thus the age of the wave packet is likely to be close to 9 days. Consequently, use of the NCEP grid point shown in Fig. 6 is warranted by the fact that the inertial oscillations generated there would be advected to the section longitude in about 5–7 days, assuming advection by the characteristic eastward frontal velocities of 20–30 cm s^{-1}, making it the closest grid point to the probable origin of the observed near-inertial wave.

The core of the wave packet extends to at least 100 m below the mixed layer, giving an estimate of 11 m day^{-1} for the mean vertical group velocity. This estimate is much higher than the theoretical prediction, based on the observed wavenumbers and stratification (4 m day^{-1}), suggesting that the wave packet slows down as it propagates into the thermocline.

Another instance of strong internal waves was seen in virtually the same location during the second front crossing, which coincidentally followed the only other significant inertial forcing event of the summer (Fig. 6d). The amplitude of the internal wave was smaller ($\sim$7 cm s^{-1}) apparently reflecting the weaker forcing, associated with the second storm.

Two other R/V *Revelle* cruises, in May–June 1999 and January–February 2000, specifically targeted processes in the subpolar front. Underway ADCP data provided to us by C. Lee (2000, personal communication) showed trapped near-inertial waves in the frontal zone on almost all cross-frontal sections, both in winter and in spring. Neither of the surveys, however, included waves of such intensity, coherence, and horizontal extent as those in June–July 1999, described above. This result is somewhat unexpected since the forcing is considerably stronger in wintertime. However, it is in agreement with the concurrent mooring observations in Korea Strait, which also show a significant decrease in inertial oscillation activity in winter (Jacobs et al. 2000). It is presently undetermined whether the particularly favorable sporadic forcing, relatively shallow mixed layer, large-scale vorticity, or advection pattern is responsible for the strong near-inertial wave manifestation in summer.

4. Depth dependence of internal wave energy and propagation

a. Mean vertical distribution of internal wave energy

The LADCP dataset obtained during the summer 1999 cruises combines relatively high vertical resolution, range to the ocean bottom, and reasonably uniform spatial coverage of the whole Japan Sea. Consequently, this dataset permits us to study the three-dimensional kinetic energy distribution and to compare the direction of energy propagation at different depths.

For this purpose the depth-dependent rotary energy spectra were computed, using a sliding window of constant width. For each sufficiently deep vertical shear profile, the rotary spectrum was calculated with the window centered every 100 m in the vertical starting at 250 m. The spectra so obtained were corrected and integrated in wavenumber space as described in section 3e, producing estimates of clockwise- and counterclockwise-polarized kinetic energies at the depths of each of the window centers.

The width of the Hanning window was chosen to be 500 m as a compromise between the vertical resolution and wavenumber space coverage. Such a relatively wide window excluded the shallow (less than 500 m) stations from consideration, reducing the number of admissible

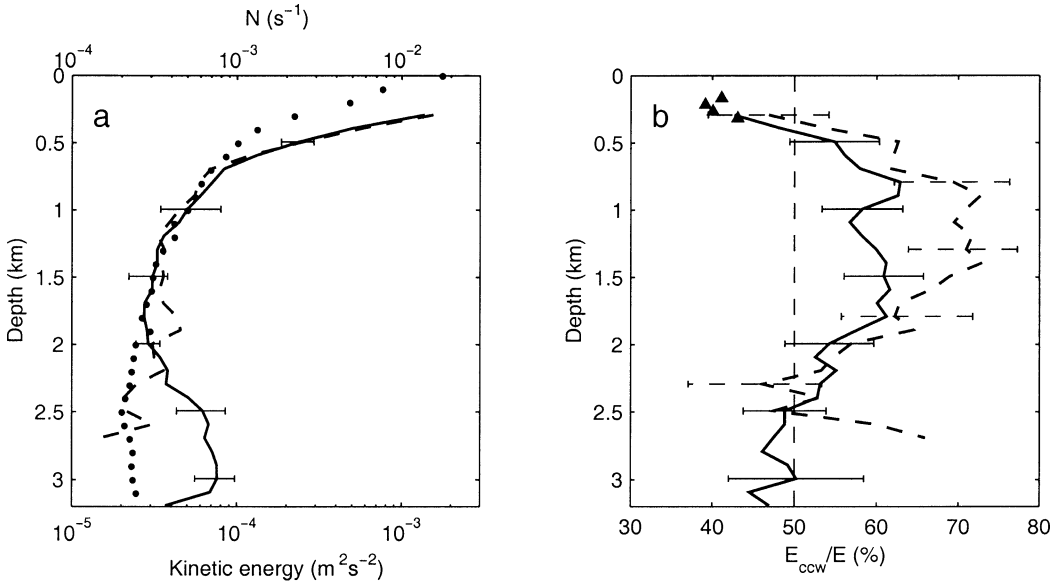

FIG. 7. (a) Mean kinetic energy, and (b) mean relative magnitude of clockwise (downward propagating) energy. Averages over the whole Japan Sea (solid line) and Yamato basin only (dashed line) are shown. Error bars represent 95% confidence intervals, estimated using bootstrap method (Zoubir and Boashash 1998). Mean buoyancy frequency is also shown in (a) by dotted line.

stations from 203 to 131. A least squares fit of a quadratic polynomial was removed from each 500-m segment of a velocity profile prior to window application in order to reduce the effects of large-scale vertical shear.

Averaged horizontally over the whole basin, the total kinetic energy decreases rapidly from 2×10^{-3} m^2 s^{-2} in the thermocline to about 3×10^{-5} m^2 s^{-2} at depth 2000 m (Fig. 7a). This change is consistent with WKB scaling, based on the buoyancy frequency change. Below 2000 m the energy rises again to about 1×10^{-4} m^2 s^{-2}. This increase could indicate topographic internal wave generation.

The counterclockwise fraction of kinetic energy crosses 50% at 500 m (Fig. 7b), indicating a reversal in the direction of net energy flux. In the upper 500 m the counterclockwise kinetic energy (E_{CCW}) accounts for less than half of the total baroclinic energy. Other calculations of energy distribution in the upper thermocline that we made using a narrower window (triangles in Fig. 7b) indicate that the relative contribution of E_{CCW} is below 40% on average, and can be as low as 8% locally (cf. Fig. 5) in the upper 300 m. As shown in section 3, such an asymmetry is an indication of net downward energy propagation. This is widely observed (e.g., Leaman 1976; D'Asaro and Perkins 1984; Kunze and Sanford 1984) and expected in the upper layers of the ocean where energetic near-inertial waves dominate the transport of wind-induced energy into the thermocline. However, we find that between 500 m and 2500 m counterclockwise energy dominates the energy balance in the Japan Sea. The maximum relative contribution of counterclockwise energy is over 60%, at depth ~1500 m.

b. Spatial variability of internal wave energy

The vertical energy distribution averaged over such an inhomogeneous region as the Japan/East Sea, with its strong currents, fronts and varying stratification, provides just an indication of the global tendencies in the sea.

As each individual vertical energy profile is inherently noisy, a large number of stations is required to attain a stable average, reducing the feasibility of regional averaging. An example of regional averaging over the 31 stations within the Yamato basin (Fig. 7b, dashed line) exhibits substantial degradation of confidence intervals when compared with the basin average. Clearly, an average over a smaller region would be dominated by the errors. Instead, empirical orthogonal function (EOF) analysis was used to investigate spatial variability of the vertical energy distribution.

The relative contribution of counterclockwise energy (E_{CCW}/E ratio) was chosen as a single variable characterizing the dominant energy propagation direction. The two-dimensional distribution of this ratio, with depth and station number as independent parameters, was decomposed in two sets of modes, characterizing its vertical and horizontal variability. The decomposition is optimal in the sense that maximum variance in each dimension can be described using a minimal number of modes from the corresponding set. The neutral value of the E_{CCW}/E ratio (0.5) has been subtracted from the data prior to the decomposition, because the goal is to study the deviations from this value. It was subsequently added back to the vertical modes for display. The dominant

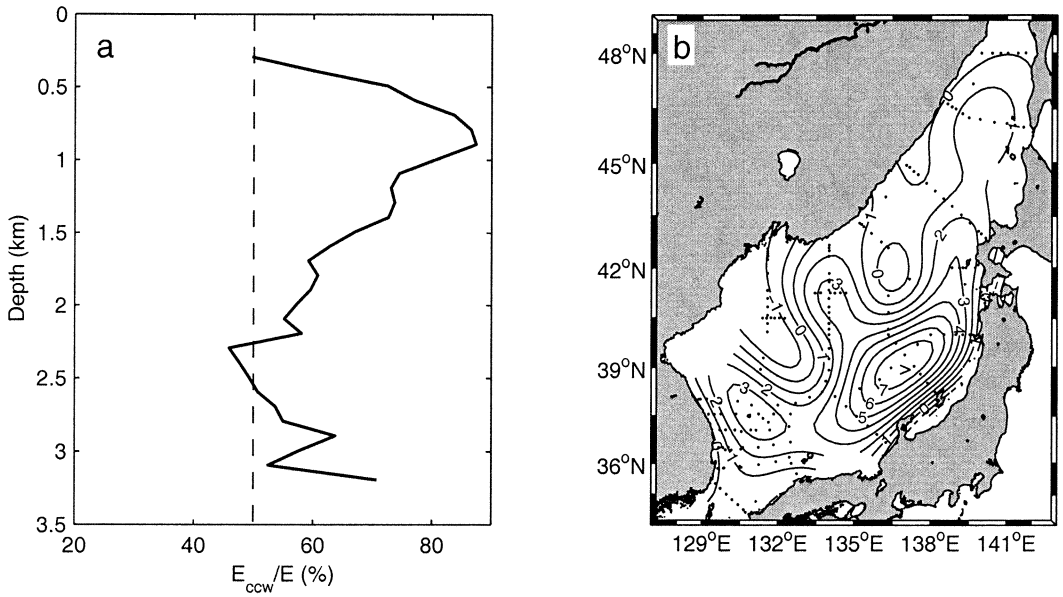

FIG. 8. Dominant (a) vertical and (b) horizontal modes of EOF-decomposition of relative magnitude of clockwise energy.

vertical mode (Fig. 8a) with the corresponding horizontal mode (Fig. 8b) describes 22% of total variance. This first vertical mode clearly captures the peak at depth 1000 m corresponding to the upper part of the broad peak seen in the basin average (Fig. 7b). As evident from Fig. 8b, the most prominent manifestation of this peak is observed in the Yamato basin in the southeastern corner of the Japan Sea.

Cross sections of relative contribution of E_{CCW} (Figs. 9a,b) allow further localization of the upward-propagating energy. The maximum values of E_{CCW}/E ratio are observed along the northern slopes of the Yamato rise and Noto peninsula, suggesting that the large-scale circulation may be the reason for the dominance of the Yamato basin in generating upward-propagating internal waves. This region is characterized by the energetic Tsushima Current flowing northeastward along the Japanese coastline, closely following the shelf break. Interaction with the rough topography in the vicinity of the Oki islands (36°N, 133°E), Oki ridge (37°N, 135°E, $<$500 m deep), and Noto peninsula (37°N, 137°E) may lead to upward-propagating energy enhancement through lee wave generation (Bell 1975). Even though the velocities in the core of Tsushima Current exceed 25 cm s^{-1}, the observed near-bottom flow is weak (a few centimeters per second) and may not be sufficient to explain the observed energy distribution.

Another possible explanation for the existence of upward-propagating energy maximum may be internal tide generation at the topographic features (e.g., Holloway and Merrifield 1999). The bottom slope at the depth of the maximum is significantly below critical for semidiurnal tides. (The ratio of bathymetry slope to the internal tide characteristics is on the order of 0.2.) However, local supercritical features not resolved by the 5′ bathymetry used may be present. Additionally, internal tide propagation from shallower supercritical regions in the vicinity of Noto peninsula may take place.

As the vertical extent of the peak in E_{CCW}/E averaged over the whole Japan Sea is considerably wider than that observed in the Yamato basin alone, multiple sites and mechanisms of counterclockwise energy generation at different depths may exist. The different mechanisms of generation of upward-propagating internal waves as well as the factors that determine the depth of the E_{CCW}/E peak requires further investigation, involving studies of the internal wave energy distribution in varying large-scale settings.

c. Comparison with other regions

In order to compare the Japan Sea with a different region of the ocean, the same analysis was applied to a subpolar North Atlantic LADCP dataset from World Ocean Circulation Experiment (WOCE) section A24 (Fig. 10b). In addition to similar latitude ranges, the North Atlantic topography resembles that of the Japan Sea: both regions have basins 3000 m deep, separated by a ridge at about 1000 m (Mid-Atlantic Ridge and Yamato rise, respectively). Additionally, the pattern of the North Atlantic current flowing northward along the western edge of the Rockall plateau is similar to that of the Tsushima Current and subpolar front impinging on the complicated topography of the Japanese coastline.

The vertical section of E_{CCW}/E from the North Atlantic (Fig. 9c) shows upward energy enhancement along the plateau slope and at the ridge, similar to the locations of high E_{CCW}/E in the Japan Sea.

A tropical Indian Ocean WOCE LADCP dataset, pro-

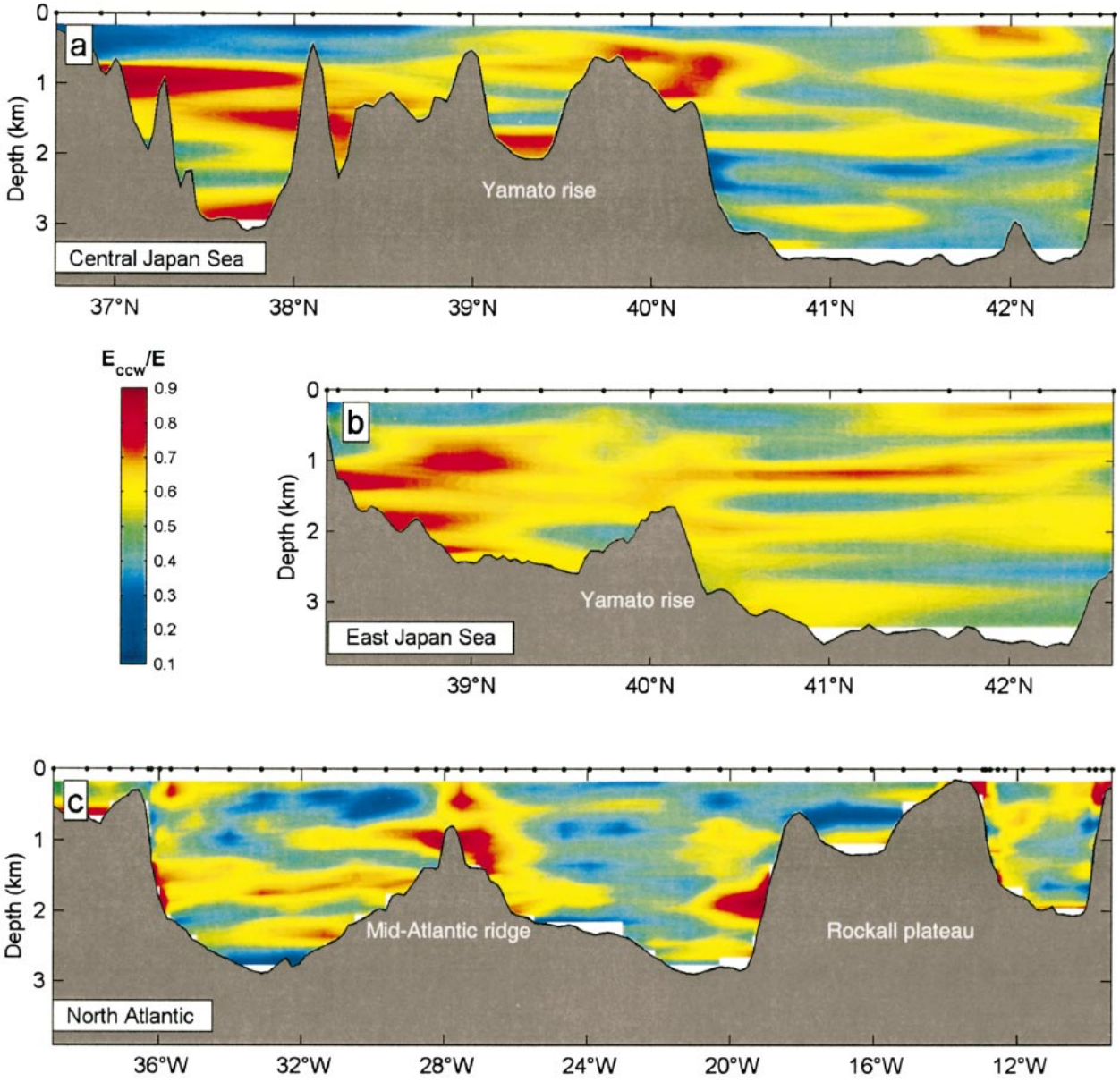

FIG. 9. Vertical sections of E_{CCW}/E ratio across (a) central and (b) eastern Japan/East Sea, and also across (c) subpolar North Atlantic. Section locations are shown in Fig. 10.

vided by T. Chereskin (2000, personal communication), was also examined (not shown). No upward deep energy propagation was apparent, suggesting that the processes at work in the deep Japan Sea and North Atlantic are not active in this particular tropical region.

5. Conclusions

The vertical distribution of internal wave energy and flux in the Japan Sea appears to be related to the stratification and topography.

Mean downward energy flux was observed in the upper 500 m of the water column. Local intensification of such flux due to strong near-inertial oscillations was found in the vicinity of the subpolar front. This intensification was consistent with the trapping of near-inertial waves by the region of negative relative vorticity, associated with the front. However, another instance of near-inertial wave trapping was found in a region of apparently positive relative vorticity, highlighting the importance of better sampling of the vorticity field than was done during the discussed survey if the near-inertial wave field is to be understood.

Net upward energy flux was found at depths between 1000 and 2000 m, and was most prominent in the Yamato basin in the southeastern part of the sea. Topo-

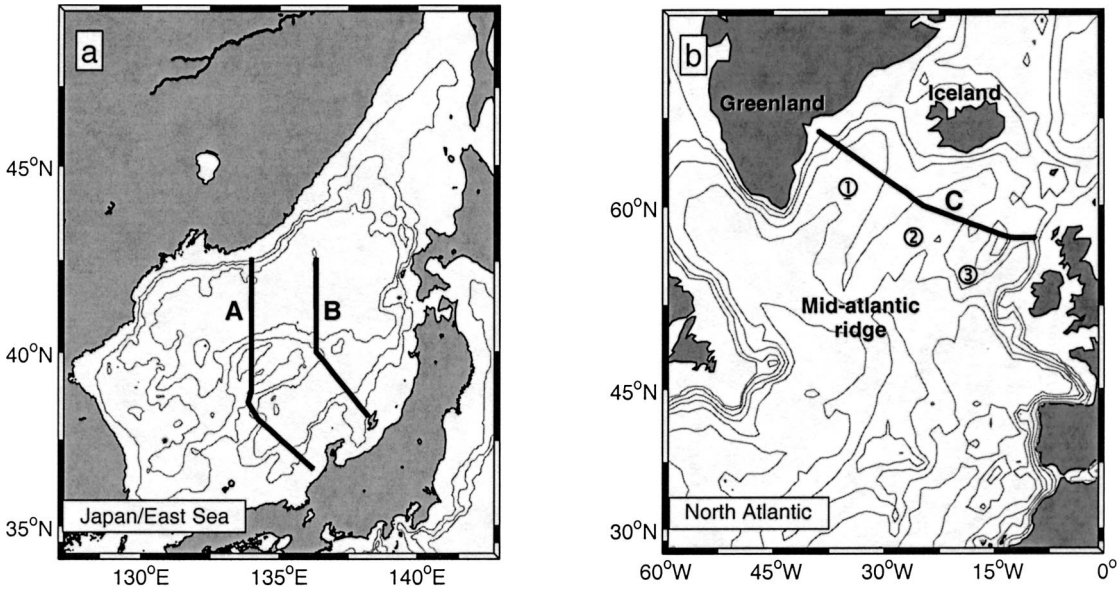

FIG. 10. Locations of the (a) Japan/East Sea and (b) North Atlantic sections, used in Fig. 9. Letters indicate Central Japan Sea section (A, Fig. 9a), East Japan Sea section (B, Fig. 9b), and WOCE North Atlantic A24 section, May–Jun 1997 (C, Fig. 9c). Numbers in (b) indicate (1) Irminger basin, (2) Iceland basin, and (3) Rockall plateau.

graphic generation of internal waves is hypothesized as one of the plausible explanations for the observed energy distribution. Testing of this hypothesis, as well as the others, including the tidal generation, has to be addressed in further investigations. Application of the analysis described in this paper to the available global LADCP dataset, acquired largely during WOCE, would be of interest for revealing regions with a vertical energy distribution similar to that observed in the Japan Sea. A short study has shown that subpolar North Atlantic is one such region. Further analysis of the similarities between these regions should provide additional insights into the processes involved.

Acknowledgments. We thank the captains, crews, and scientific staffs aboard the R/V *Revelle* and R/V *Khromov*, Y. Volkov of the Far Eastern Regional Hydrometeorological Research Institute for arranging the Khromov cruise and V. Luchin as chief scientist of that cruise, and SIO Oceanographic Data Facility. We are also grateful to C. Lee for making available ADCP data for the winter and spring cruises, T. Chereskin for providing Indian Ocean WOCE LADCP data, R. Pinkel and M. Alford for helpful and stimulating discussion.

AVHRR SST imagery was provided by R. Arnone and S. Ladner (Naval Research Laboratory, Stennis Space Center). NCEP reanalysis data were provided by the NOAA–CIRES Climate Diagnostics Center, Boulder, Colorado, from their Web site online at http://www.cdc.noaa.gov/. Maps were produced with the MMAP package.

The present study is supported by Office of Naval Research Grant ONR N00014-98-1-0220.

APPENDIX

Confidence Intervals for (L)ADCP Spectral Analysis

The vertical wavenumber spectra discussed in section 3d are estimated from a series of shipboard ADCP profiles. Because of the relatively high sampling rate (once every 5 min) and the remarkable horizontal coherence of the observed internal wave field, the adjacent velocity profiles cannot be considered statistically independent. Consequently, the effective number of degrees of freedom M of the mean vertical wavenumber spectra, obtained by averaging of the spectra of N individual profiles, is much lower than the formal estimate of $2N$ and may also depend on vertical wavenumber k:

$$M(k) = \frac{2N^2}{\sum_{i,j} \gamma_{ij}^2(k)}, \tag{A1}$$

(D'Asaro and Perkins 1984) where $\gamma_{ij}(k)$ is the coherence of the profiles i and j. The amount of data available does not allow the calculation of the full coherence matrix $\gamma_{ij}(k)$ for the lowest vertical wavenumbers. However, assuming the statistics are stationary so that for each wavenumber, $\gamma_{ij}(k) = \gamma(k, |r_{ij}|)$ is only a function of spatial separation $|r_{ij}|$ between the profiles i and j, and that the sampling is regular with the spacing Δr, so that $|r_{ij}| = \Delta r|i - j|$, (A1) can be simplified:

$$M = \frac{2N^2}{\sum_{m=-N}^{N} (N - m)\gamma_m^2(k)}, \tag{A2}$$

where $\gamma_m(k) = \gamma(k, m\Delta r)$ can be estimated from the autocorrelation of the vertical Fourier transforms $\hat{V}_i(k)$ of the velocity profiles:

$$\gamma_m = \frac{|\langle \hat{V}_i^* \hat{V}_{i+m} \rangle|}{\langle |\hat{V}_i| \rangle^2},$$

where averaging over N profiles is shown by angle brackets and the asterisk denotes complex conjugate.

The effective number of degrees of freedom M estimated using (A2) was the smallest for the highly correlated clockwise component, being only 6–8 for the wavelengths of 50 m and longer. For short counterclockwise wavenumbers of the same wavelengths M was between 11 and 20. For higher wavenumbers of both polarizations it increased to about 80, which is, however, still much lower than the formal estimate (196) because of the spurious coherence of the noise.

Confidence intervals can then be calculated using the χ^2 distribution with M degrees of freedom. Only the confidence interval based on the effective number of degrees of freedom for the *clockwise* component is shown in Fig. 4. The confidence interval for the *counterclockwise* component has similar wavenumber dependency but is 20%–50% narrower. The confidence interval based on the formal number of degrees of freedom is also shown for comparison purposes.

Clockwise and counterclockwise energies discussed in section 3e (Fig. 5) are obtained by frequency integration of rotary spectra of individual (L)ADCP velocity profiles. Monte Carlo simulation of E_{CW} and E_{CCW} distribution was used to compute the corresponding confidence intervals. For that purpose the mean wavenumber spectrum $S_0(k_z)$ was calculated from the data, and then a large number of random spectra $S_i(k_z)$ were generated so that the ratio $S_i(k_z)/S_0(k_z)$ obeys χ^2 distribution with 2 degrees of freedom, consistent with the expected distribution of spectral estimates, provided $S_0(k_z)$ is the true process spectrum. Each of the spectra was then integrated and the distributions of E_i/E_0 (for clockwise and counterclockwise energies separately) were studied. All distributions closely followed the χ^2 law, with the effective number of degrees of freedom ranging from about 9 for E_{CCW} to 12 for E_{CW}. The distributions were very close for ADCP and LADCP data, even though the formal number of degrees of freedom would be significantly different (31 and 51 correspondingly). For clarity, only the ''mean'' confidence interval, calculated using χ^2 distribution with 11 degrees of freedom is shown in Fig. 5. The confidence interval for 9 degrees of freedom would be about 10% wider.

REFERENCES

Alford, M., 2001: Internal swell generation: The spatial distribution of energy flux from the wind to mixed layer near-inertial motions. *J. Phys. Oceanogr.,* **31,** 2359–2368.

Bell, T. H., 1975: Topographically generated internal waves in the open ocean. *J. Geophys. Res.,* **80,** 320–327.

D'Asaro, E. A., and H. Perkins, 1984: A near-inertial wave spectrum for the Sargasso Sea in late summer. *J. Phys. Oceanogr.,* **14,** 489–505.

Firing, E., and R. Gordon, 1990: Deep ocean acoustic Doppler current profiling. *Proc. IEEE Fourth Working Conf. on Current Measurements*, Clinton, MD, IEEE, 192–201.

Fischer, J., and M. Visbeck, 1993: Deep velocity profiling with self-contained ADCPs. *J. Atmos. Oceanic Technol.,* **10,** 764–773.

Fomin, L. M., 1973: Inertial oscillations in a horizontally inhomogeneous current velocity field. *Izv. Atmos. Oceanic Phys.,* **9,** 75–83.

Holloway, P., and M. Merrifield, 1999: Internal tide generation by seamounts, ridges, and islands. *J. Geophys. Res.,* **104,** 25 937–25 951.

Jacobs, G. A., W. J. Teague, H. T. Perkins, S. K. Riedlinger, and R. H. Preller, 2000: Inertial oscillations in the Korea/Tsushima Strait. *Eos, Trans. Amer. Geophys. Union,* **81,** F765–F766.

Kunze, E., 1985: Near-inertial wave propagation in geostrophic shear. *J. Phys. Oceanogr.,* **15,** 544–565.

——, and T. B. Sanford, 1984: Observations of near-inertial waves in a front. *J. Phys. Oceanogr.,* **14,** 566–581.

Large, W. G., and S. Pond, 1981: Open ocean momentum flux measurements in moderate to strong winds. *J. Phys. Oceanogr.,* **11,** 324–336.

Leaman, K. D., 1976: Observations on the vertical polarization and energy flux of near-inertial waves. *J. Phys. Oceanogr.,* **6,** 894–908.

——, and T. B. Sanford, 1975: Vertical energy propagation of internal waves: A vector spectral analysis of velocity profiles. *J. Geophys. Res.,* **80,** 1975–1978.

Mied, R. P., C. Y. Shen, C. L. Trump, and G. J. Lindermann, 1986: Internal-inertial waves in a Sargasso Sea front. *J. Phys. Oceanogr.,* **16,** 1751–1762.

Mooers, C. N. K., 1975a: Several effects of a baroclinic current on the cross-stream propagation of inertial-internal waves. *Geophys. Fluid Dyn.,* **6,** 245–275.

——, 1975b: Several effects of a baroclinic current on the three-dimensional propagation of inertial-internal waves. *Geophys. Fluid Dyn.,* **6,** 277–284.

Olbers, D. J., 1981: The propagation of internal waves in a geostrophic current. *J. Phys. Oceanogr.,* **11,** 1224–1233.

Perkins, H., W. Teague, G. Jacobs, K. Chang, and M. Suk, 2000: Currents in Korea–Tsushima Strait during summer 1999. *Geophys. Res. Lett.,* **27,** 3033–3036.

Polzin, K., E. Kunze, J. Hummon, and E. Firing, 2002: The finescale response of lowered ADCP velocity profiles. *J. Atmos. Oceanic Technol.,* **19,** 205–224.

Takematsu, M., J.-H. Yoon, A. Masuda, and J. Na, 1999a: CREAMS: Circulation Research of the East Asian Marginal Seas. *J. Oceanogr.,* **55,** 101–382.

——, Z. Nagano, A. Ostrovskii, K. Kim, and Y. Volkov, 1999b: Direct measurements of deep currents in the northern Japan Sea. *J. Oceanogr.,* **55,** 207–216.

Talley, L. D., 1991: An Okhotsk water anomaly: Implications for ventilation in the North Pacific. *Deep-Sea Res.,* **38** (Suppl), S171–S190.

Zoubir, A. M., and B. Boashash, 1998: The bootstrap and its application in signal processing. *IEEE Sig. Proc. Mag.,* **15** (1), 56–76.